WILEY | Hindawi

Research Article

IBOA-Based Optimization of Cross-Sectional Dimension of Rods for a 3-RRR PPM to Minimize Energy Consumption

Yin Gao [ID],[1,2] **Ke Chen,**[1] **Hong Gao,**[2] **Hongmei Zheng,**[1] **Lei Wang,**[2] **and Kerong Jiang**[3]

[1]*School of Mechanical Engineering, Hefei University of Technology, Hefei 230009, China*
[2]*School of Mechanical Engineering, Anhui Polytechnic University, Wuhu 241000, China*
[3]*School of Advanced Manufacturing Engineering, Hefei University, Hefei 230601, China*

Correspondence should be addressed to Yin Gao; gy0203@mail.hfut.edu.cn

For obtaining optimal cross-sectional dimensions of rods for a 3-RRR planar parallel manipulator (PPM) to minimize energy consumption, the inverse dynamics of the manipulator is modeled based on the Newton–Euler method, after which the coefficient matrix of the inverse dynamics equation is decomposed based on matrix theory. Hence, the objective function, that is, the logical relationship between the energy consumption of the manipulator and the cross-sectional dimension of each rod, is established. However, in solving the multidimensional constrained single-object optimization problem, there are difficulties such as the penalty function's sensitivity to the penalty factors if the problem is transformed into the one of unconstrained multiobjective optimization. Therefore, to properly handle the constraints, an improved butterfly optimization algorithm (IBOA) is presented to ensure that the new iterated point always falls into the feasible region according to the butterfly optimization algorithm (BOA). Finally, the comparisons among the IBOA, particle swarm optimization (PSO), and BOA and further experiments of the physical prototype are implemented to validate the effectiveness of the proposed theoretical model and numerical algorithm. Results indicate that the proposed IBOA is more suitable for solving the constrained single-object optimization problem with better convergence speed and accuracy.

1. Introduction

A 3-RRR planar parallel manipulator (PPM) is a type of manipulator with only three degrees of freedom, in which the symbol 3-RRR expresses three branched chains and includes three revolute (R) pairs in each branched chain, which has the advantages of a simple structure, small additional inertia of the driving motor, large stiffness, large workspace, and small cumulative error. It has been widely used in the fields of plane complex curve creation [1], micro-nano-precision positioning, measurement, and manufacturing [2, 3], pick and place operation robots [4, 5], modular, detachable, and reconfigurable robots [6], tactile perception [7, 8], and additive manufacturing equipment [9, 10].

When the length of each rod is known, the shape, size range, and singular point distribution of the workspace of the 3-RRR PPM are determined by inverse kinematics and workspace analysis [11]. However, the selection of the cross-sectional dimension of each rod will inevitably affect its mass distribution and the dynamic indexes, such as rotational inertia and inertial force (moment) of each rod, which will eventually affect the energy consumption of the manipulator.

The dynamics is the necessary foundation for energy consumption research. There are some classical methods for the dynamic modeling of parallel mechanisms based on multirigid-body dynamics theory, such as the principle of virtual work [12–14], Kane's equations [15], Lagrange method [5, 16–18], and Newton–Euler method [19–24].

Although the dynamic modeling of the 3-RRR PPM can choose the methods of Kane or Lagrange, the Newton–Euler method can not only establish its inverse dynamic model but also obtain the relationship between the driving torque and

the movement time, as well as the internal force of the hinge and the movement time [24].

In general, after the usage of the manipulator is determined, its motion path in the workspace is determined. In this situation, the optimal masses of each rod can be determined by establishing an optimization model to optimize the energy consumption [21]. For the 3-RRR PPM, the masses of the connecting rods and moving platform were selected as variables (seven variables in total), and the energy consumption of the driving motor was considered as the objective function. Finally, the optimization model is solved using the particle swarm method. However, for the 3-RRR PPM with asymmetric dimensional parameters, even for similar energy consumption optimization problems, it will face three challenges owing to the increase in rectangular cross-sectional parameters: (1) calculation of the objective function, that is, the relationship between the energy consumption of the driving motor and the motion path of the moving platform or the movement time; (2) selection of numerical method, that is, how to seek numerical methods to meet the requirements of the speed and accuracy of convergence and global optimization; (3) handling of constraints.

As aforementioned, once the inverse dynamics model of the 3-RRR PPM is established based on the Newton–Euler method, its inverse dynamics solution can be expressed as a matrix equation. It can be seen from the matrix equation that the inverse dynamic solution, such as the driving torque of the active motor, is closely related to the cross-sectional dimension of each rod. However, the coefficient matrix is only related to the length of each rod, position and orientation of the moving platform, and dynamic displacement of each rod but is not related to the cross-sectional dimension of each rod. This property means that, through the QR decomposition of the coefficient matrix [25], a logical relationship can be established between the energy consumption of the manipulator and the cross-sectional dimension of each rod.

In recent years, the metaheuristic algorithms have been widely used in solving different optimization problems. In one study [26], summarizing the development history of the metaheuristic or nature inspired algorithms for the last thirty years, Mohamed et al. divided the metaheuristic algorithms into four categories such as evolutionary techniques enlightened by biology, swarm intelligence techniques enlightened by the behavior of social insects or animals, physics-based techniques enlightened by the rules governing a natural phenomenon, and human-related techniques enlightened by body activities or mind activities of the human being. Furthermore, a novel creative algorithm called gaining sharing knowledge-based algorithm (GSK) was proposed to solve optimization problems [26]. In fact, hybridizing different algorithms to benefit from each other is an important method. In that respect, Deng et al. [27–29] have made a fruitful contribution: on the basis of the MSIQDE that is an improved quantum-inspired differential evolution (QDE) with a multistrategy algorithm, an enhanced MSIQDE algorithm based on mixing multiple strategies, namely, EMMSIQDE, was presented to address

the probable premature convergence, reduced searchability, and trapping in local optima in the QDE [27]; an improved quantum evolutionary algorithm (QEA) based on the niche coevolution strategy and enhanced PSO, namely, IPOQEA, was proposed to solve the three-objective gate allocation model [28]; similarly, QEA and cooperative coevolution evolutionary algorithm (CCEA) were combined to improve the weakness of differential evolution algorithm (DEA) during the solution of the large-scale complex optimization problem. An effective HMCFQDE algorithm based on the CC framework, QEA, and hybrid mutation strategy was presented and established [29]. Besides, the butterfly optimization algorithm (BOA) proposed by Arora and Singh [30, 31] is also worth substantial attention. After 30 different benchmark functions and 7 widely used metaheuristic algorithms, which included artificial bee colony (ABC), cuckoo search (CS), differential evolution (DE), firefly algorithm (FA), genetic algorithm (GA), monarch butterfly optimization (MBO), and PSO, being chosen and compared from the view of the statistical assessment for benchmarking the performance of BOA, 6 familiar engineering problems were solved by BOA. Therefore, the conclusion that BOA can become an effective tool to solve real-world optimization problems was reached [31]. Nevertheless, the advantages of BOA in solving engineering optimization problems are what we are most interested in.

In addition, for the problem of constrained single-object optimization, the handling of constraints is used by changing the constrained single-object optimization to unconstrained multiobjective optimization through the introduction of the constraints in the objective function [32–34]. However, there are also difficulties in implementation; for example, the main drawback of the introduction of the penalty function in the objective function is that the penalty function is exceedingly sensitive to the penalty factors [33]. Therefore, to address the problem of the optimal cross-sectional dimension of rods for the 3-RRR PPM to minimize energy consumption, an improved butterfly optimization algorithm (IBOA) is presented to properly handle the constraints of the single-object optimization problem by ensuring that the iteration point always falls into the feasible region.

The rest of the paper is organized as follows. In Section 2, the inverse dynamic equations based on the Newton–Euler method are derived, and the detailed process of QR decomposition of the coefficient matrix of the equations is provided. In Section 3, considering the length and width of the rectangular cross-sectional dimension of each rod for the 3-RRR PPM as the variable, the energy consumption of the driving motor as the objective function, and the upper and lower limits of the cross-sectional dimension of each rod as the constraint, the model of the optimal cross-sectional dimension of rods to minimize energy consumption is established. Meanwhile, after the objective function, that is, the logical relationship between the energy consumption of the manipulator and the cross-sectional dimension of each rod is revealed, the algorithm and flowchart for solving the problem of optimal cross-sectional dimension of the rod based on IBOA are presented. In Section 4, the optimization

results of an example are presented and verified experimentally. Finally, the paper is concluded in Section 5.

2. Dynamics for the 3-RRR PPM

2.1. Modeling of Dynamics. As is shown in Figure 1(a), there are three branched chains $A_iB_iC_i$ ($i = 1, 2, 3$ in this paper) connected between the moving platform and the frame, each of which has two rods, A_iB_i and B_iC_i, and three revolute pairs, A_i, B_i, and C_i. One end of the three branched chains is connected to the frame at point A_i, and the other end is connected to the moving platform triangle $C_1C_2C_3$ at point C_i.

For the convenience of kinematics and dynamics analysis, as shown in Figures 1(a) and 1(b), the global coordinate system oxy is established on the frame triangle $A_1A_2A_3$, and the center o of the circumscribed circle of triangle $A_1A_2A_3$ is considered as the coordinate origin, such that the x-axis is parallel to A_2A_3 and the y-axis passes through point o. The positive direction is determined using the right-hand rule. The local coordinate system $G_7x'y'$ is established on triangle $C_1C_2C_3$, and the center G_7 of the circumscribed circle of triangle $C_1C_2C_3$ is considered as the coordinate origin, such that the x' axis is parallel to C_2C_3 and the y' axis passes through point G_7. The positive direction is determined by the right-hand rule.

For easy reference, the meaning and symbol of dimension parameters, kinematics, and dynamics parameters for the 3-RRR PPM are listed in Table 1 in Appendix A.

When the inverse displacements θ_i of the 3-RRR PPM are solved, the known conditions are as follows: the global coordinate (x, y) of the central point G_7 of the moving platform and orientation angle θ of the moving platform; dimension parameters, including the lengths l_i of the active rods A_iB_i, lengths l_{i+3} of the passive rod B_iC_i, lengths a, b, and c of sides of frame triangle $A_1A_2A_3$, and lengths d, e, and f of the sides of the moving platform triangle $C_1C_2C_3$, as shown in Figure 1(a). Based on the theory of mechanism, the angular displacements of the active parts can be calculated [11]:

$$\theta_i = 2 \tan^{-1} \frac{N_i \pm \sqrt{N_i^2 + M_i^2 - K_i^2}}{M_i + K_i}, \quad i = 1, 2, 3. \quad (1)$$

Meanwhile, the condition that the solution of equation (1) is a real number is

$$N_i^2 + M_i^2 \geq K_i^2, \quad i = 1, 2, 3. \quad (2)$$

Here,

$$M_i = x + x'_{ci} \cos \theta - y'_{ci} \sin \theta - x_{Ai}, \quad i = 1, 2, 3,$$

$$N_i = y + x'_{ci} \sin \theta + y'_{ci} \cos \theta - y_{Ai}, \quad i = 1, 2, 3, \quad (3)$$

$$K_i = \frac{M_i^2 + N_i^2 + l_i^2 - l_{i+3}^2}{2l_i}, \quad i = 1, 2, 3.$$

The parameters that are not listed above are presented in Appendix B, equations (B.1)–(B.6).

For the inverse dynamics modeling based on the Newton–Euler method for the 3-RRR PPM, in addition to the conditions given in the previous inverse displacement solution, the remaining known conditions are as follows: the masses m_{Gi} of the active rod A_iB_i, masses $m_{G\,(i+3)}$ of the passive rod B_iC_i, mass m_{G7} of the moving platform, external forces F_{ex} and F_{ey} of the moving platform, and external moment M_e of the moving platform. The solving goal is as follows: the internal forces F_{Bix} and F_{Biy} at point B_i, internal forces F_{Cix} and F_{Ciy} at point C_i, and the driving moment of the active rod A_iB_i. As shown in Figure 1(b), the active rod A_iB_i, passive rod B_iC_i, and moving platform triangle $C_1C_2C_3$ are considered isolators. The inverse dynamics modeling for the 3-RRR PPM can be expressed as the following matrix [24]:

$$\mathbf{Ax} = \mathbf{B}, \quad (4)$$

where

$$x = \begin{bmatrix} x_1 \\ x_2 \\ \dots \\ x_{15} \end{bmatrix},$$

$$= \begin{bmatrix} F_{C1x} & F_{C2x} & F_{C3x} & F_{C1y} & F_{C2y} & F_{C3y} & F_{B1x} & F_{B2x} & F_{B3x} & F_{B1y} & F_{B2y} & F_{B3y} & \tau_1 & \tau_2 & \tau_3 \end{bmatrix}^T,$$

$$\mathbf{A} = \begin{bmatrix} a_{11} & a_{12} & \dots & a_{1,15} \\ a_{21} & a_{22} & \dots & a_{2,15} \\ \dots & \dots & \dots & \dots \\ a_{21,1} & a_{21,2} & \dots & a_{21,15} \end{bmatrix},$$

$$\mathbf{B} = \begin{bmatrix} B_1 \\ B_2 \\ \dots \\ B_{21} \end{bmatrix}. \quad (5)$$
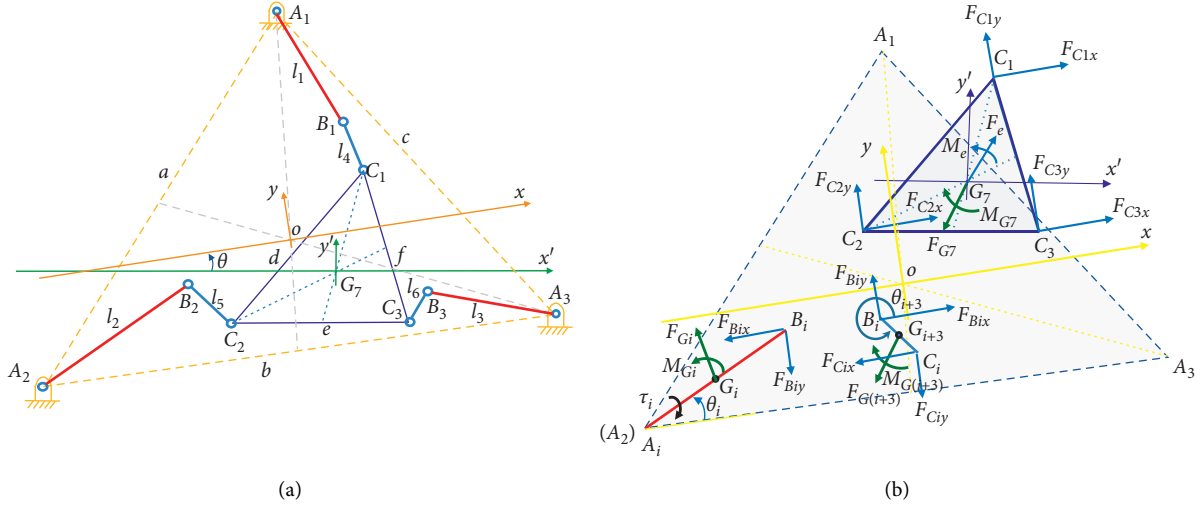
(a)

(b)

FIGURE 1: Schematic diagram of the 3-RRR PPM and dynamics modeling. (a) Schematic diagram of the 3-RRR PPM. (b) Process of the dynamics modeling.

Here, $\mathbf{A} \in \mathbb{R}^{21 \times 15}$ is a sparse matrix, and the nonzero elements are [24] $a_{11} = a_{12} = a_{13} = a_{24} = a_{25} = a_{26} = a_{47} = a_{58} = a_{69} = a_{7,10} = a_{8,11} = a_{9,12} = a_{13,7} = a_{14,8} = a_{15,9} = a_{16,10} = a_{17,11} = a_{18,12} = 1$; $a_{41} = a_{52} = a_{63} = a_{74} = a_{85} = a_{96} = a_{19,13} = a_{20,14} = a_{20,15} = -1$; $a_{31} = -|y - y_{C1}|$, $a_{32} = |y - y_{C2}|$, $a_{33} = |y - y_{C3}|$, $a_{34} = |x - x_{C1}|$, $a_{35} = -|x - x_{C2}|$, $a_{36} = |x - x_{C3}|$; $a_{10,1} = -|y_{G4} - y_{C1}|$, $a_{10,4} = -|x_{G4} - x_{C1}|$, $a_{10,7} = -|y_{G4} - y_{B1}|$, $a_{10,10} = -|x_{G4} - x_{B1}|$; $a_{11,2} = -|y_{G5} - y_{C2}|$, $a_{11,5} = -|x_{G5} - x_{C2}|$, $a_{11,8} = -|y_{G5} - y_{B2}|$, $a_{11,11} = -|x_{G5} - x_{B2}|$; $a_{12,3} = -|y_{G6} - y_{C3}|$, $a_{12,6} = -|x_{G6} - x_{C3}|$, $a_{12,9} = -|y_{G6} - y_{B3}|$, $a_{12,12} = -|x_{G6} - x_{B3}|$; $a_{19,7} = l_1 \sin\theta_1/2$, $a_{19,10} = -l_1 \cos\theta_1/2$; $a_{20,8} = l_2 \sin\theta_2/2$, $a_{20,11} = -l_2 \cos\theta_2/2$; $a_{21,9} = l_3 \sin\theta_3/2$, $a_{21,12} = -l_3 \cos\theta_3/2$.

The remaining elements that are not listed above in matrix $\mathbf{A}$ were 0.

Further, $\mathbf{B} \in \mathbb{R}^{21 \times 1}$ is a column vector whose elements include [24] $B_1 = F_{G7x} - F_{ex}$; $B_2 = F_{G7y} - F_{ey}$; $B_3 = M_{G7} - M_e$; $B_4 = F_{G4x}$; $B_5 = F_{G5x}$; $B_6 = F_{G6x}$; $B_7 = F_{G4y}$; $B_8 = F_{G5y}$; $B_9 = F_{G6y}$; $B_{10} = M_{G4}$; $B_{11} = M_{G5}$; $B_{12} = M_{G6}$; $B_{13} = -F_{G1x}$; $B_{14} = -F_{G2x}$; $B_{15} = -F_{G3x}$; $B_{16} = F_{G1y}$; $B_{17} = F_{G2y}$; $B_{18} = F_{G3y}$; $B_{19} = -M_{G1}$; $B_{20} = -M_{G2}$; $B_{21} = -M_{G3}$.

The parameters that are not listed above are presented in Appendix B, equations (B.7)–(B.25).

2.2. Numerical Solving for Dynamical Model of the 3-RRR PPM Based on QR Decomposition. Equation (4) can be solved using the QR decomposition method [25], and for the sparse matrix $\mathbf{A} \in \mathbb{R}^{21 \times 15}$, we can seek an invertible matrix $\mathbf{R} \in \mathbb{R}^{15 \times 15}$, and matrix A can be decomposed as follows:

$$\mathbf{A} = \mathbf{QR}, \tag{6}$$

where $\mathbf{Q} \in \mathbb{R}^{21 \times 15}$.

For ease of expression, let $\mathbf{a}_l$ ($l = 1, 2, 3, \ldots, 15$) be the vector of the column elements in matrix $\mathbf{A}$:

$$
\begin{aligned}
\mathbf{a}_1 &= \begin{bmatrix} a_{11} & a_{21} & a_{31} & \ldots & a_{21,1} \end{bmatrix}^T, \\
\mathbf{a}_2 &= \begin{bmatrix} a_{12} & a_{22} & a_{32} & \ldots & a_{21,2} \end{bmatrix}^T, \\
\mathbf{a}_3 &= \begin{bmatrix} a_{13} & a_{23} & a_{33} & \ldots & a_{21,3} \end{bmatrix}^T, \\
\mathbf{a}_{15} &= \begin{bmatrix} a_{1,15} & a_{2,15} & a_{3,15} & \ldots & a_{21,15} \end{bmatrix}^T.
\end{aligned}
\tag{7}
$$

Let

$$\mathbf{Q} = \begin{bmatrix} \mathbf{q}_1 & \mathbf{q}_2 & \cdots & \mathbf{q}_{15} \end{bmatrix}. \tag{8}$$

The vector $\mathbf{a}_l$ ($l = 1, 2, 3, \ldots, 15$) is orthogonalized based on the Gram–Schmidt orthogonalization method; that is, based on the 15 column vectors, the unit vectors that are orthogonal to each other are generated according to the following rules.

First, vector $\mathbf{a}_1$ is orthogonalized and denoted as $\mathbf{q}_1$:

$$
\begin{cases}
R_{11} = \|\mathbf{a}_1\|, \\
\mathbf{q}_1 = \dfrac{\mathbf{a}_1}{R_{11}}.
\end{cases}
\tag{9}
$$

Second, the vector components parallel to $\mathbf{a}_1$ are removed from $\mathbf{a}_2$, and $\mathbf{q}_2$ is orthogonalized.

$$
\begin{cases}
R_{12} = \mathbf{q}_1^T \mathbf{a}_2, \\
R_{22} = \|\mathbf{a}_2 - \mathbf{q}_1 R_{12}\|, \\
\mathbf{q}_2 = \dfrac{\mathbf{a}_2 - \mathbf{q}_1 R_{12}}{R_{22}}.
\end{cases}
\tag{10}
$$

Third, the vector components parallel to $\mathbf{a}_1$ and $\mathbf{a}_2$ are removed from $\mathbf{a}_3$, and $\mathbf{q}_3$ is orthogonalized.

$$
\begin{cases}
R_{13} = \mathbf{q}_1^T \mathbf{a}_3, \\[2mm]
R_{23} = \mathbf{q}_2^T \mathbf{a}_3, \\[2mm]
R_{33} = \left\| \mathbf{a}_3 - \mathbf{q}_1 R_{13} - \mathbf{q}_2 R_{23} \right\|, \\[2mm]
\mathbf{q}_3 = \dfrac{\mathbf{a}_3 - \mathbf{q}_1 R_{13} - \mathbf{q}_2 R_{23}}{R_{33}}.
\end{cases}
\tag{11}
$$

Similarly, for $\mathbf{q}_m$ $(2 \le m \le 15)$, there are

$$
R_{j\prime m} = \mathbf{q}_j^T \mathbf{a}_m, \quad 1 \le j\prime \le m - 1,
$$

$$
R_{mm} = \left\| \mathbf{a}_m - \sum_{j\prime=1}^{m-1} \mathbf{q}_{j\prime} R_{j\prime m} \right\|,
\tag{12}
$$

$$
\mathbf{q}_m = \frac{\mathbf{a}_m - \sum_{j\prime=1}^{m-1} \mathbf{q}_{j\prime} R_{j\prime m}}{R_{mm}}.
$$

It can be proved that $\mathbf{q}_l$ $(1 \le l \le 15)$ is a group of standard orthogonal bases in the above transformation; that is,

$$
\mathbf{q}_l^T \mathbf{q}_{l\prime} = \begin{cases} 1, & l = l', \\ 0, & l \ne l', \end{cases} \quad 1 \le l, l' \le 15.
\tag{13}
$$

Therefore,

$$
\mathbf{Q}^T \mathbf{Q} = \mathbf{I}_{15},
\tag{14}
$$

where $\mathbf{I}_{15} \in \mathbb{R}^{15 \times 15}$ is the unit matrix. This is obtained from equation (6):

$$
\mathbf{R} = \mathbf{Q}^T \mathbf{A}.
\tag{15}
$$

Equation (4) can be reduced to a simple solution form:

$$
\mathbf{Rx} = \mathbf{Q}^T \mathbf{B}.
\tag{16}
$$

Therefore,

$$
\mathbf{x} = \mathbf{R}^{-1} \mathbf{Q}^T \mathbf{B}.
\tag{17}
$$

Because matrices $\mathbf{A}$ and $\mathbf{B}$ are known, matrix $\mathbf{Q}$ can be calculated using equations (9)–(12), and then $\mathbf{x}$ can be calculated using equations (15) and (17).

3. Model and Solving of Optimal Cross-Sectional Dimension of Rods

3.1. Model of Optimal Cross-Sectional Dimension of Rods for the 3-RRR PPM to Minimize Energy Consumption. For the 3-RRR PPM, the lengths and widths of the rectangular cross section of the active rod $A_i B_i$ are u_i and v_i; lengths and widths of the rectangular cross section of the passive rod $B_i C_i$ are u_{i+3} and v_{i+3}; lengths and widths of the rectangular cross section of the three rods of the moving platform are u_7 and v_7, respectively. The mass of the active rod $A_i B_i$ is as follows:

$$
m_{Gi} = \rho u_i v_i l_i.
\tag{18}
$$

where ρ is the density of the material and the mass of the passive rod $B_i C_i$ is as follows:

$$
m_{G(i+3)} = \rho u_{i+3} v_{i+3} l_{i+3}.
\tag{19}
$$

The mass of the moving platform is as follows:

$$
m_{G7} = \rho u_7 v_7 (d + e + f).
\tag{20}
$$

According to equations (B.23)–(B.25), the rotary inertia J_{Gi} around the centroidal axis of the active rod $A_i B_i$, rotary inertia $J_{G(i+3)}$ around the centroidal axis of the passive rod $B_i C_i$, and rotary inertia J_{G7} around the centroidal axis of the moving platform are related to the length and width of the rectangular cross section of the rods. Furthermore, according to equations (B.17)–(B.22), F_{Gix}, F_{Giy}, $F_{G(i+3)x}$, $F_{G(i+3)y}$, F_{G7x}, F_{G7y}, M_{Gi}, $M_{G(i+3)}$, and M_{G7} are related to the length and width of the rectangular cross section of the rods. Therefore, matrix $\mathbf{B}$ is related to u_1–u_7 and $v_1 - v_7$, but matrix $\mathbf{A}$ is not.

When center G_7 of the mass of the moving platform moves with time $t \in [t_0, t_n]$ during the running of the 3-RRR PPM, the centroid trajectory is expressed as follows:

$$
\begin{cases} x = f_1(t), \\ y = f_2(t), \end{cases} \quad t \in [t_0, t_n].
\tag{21}
$$

The energy consumption corresponding to the interval $[t_0, t_n]$ of the movement time satisfies [21, 24]

$$
E(t) = \int_{t_0}^{t} \sum_{i=1}^{3} |\tau_i \omega_i| \, dt, \quad t \in [t_0, t_n],
\tag{22}
$$

where ω_i is the angular velocity of the active rod $A_i B_i$ and τ_i is the driving moment of the active rod $A_i B_i$. According to equation (17), τ_i can be obtained from the thirteenth, fourteenth, and fifteenth row of the vector $\mathbf{x}$; therefore, $E(t)$ in equation (22) is a function of u_1–u_7 and $v_1 - v_7$.

Let

$$
\mathbf{w} = \begin{bmatrix} u_1 & v_1 & u_2 & v_2 & u_3 & v_3 & u_4 & v_4 & u_5 & v_5 & u_6 & v_6 & u_7 & v_7 \end{bmatrix}^T.
\tag{23}
$$

Therefore, the model of the optimal cross-sectional dimension of the rods for the 3-RRR PPM to minimize energy consumption is

$$
\min E(\mathbf{w}) = \int_{t_0}^{t} \sum_{i=1}^{3} |\tau_i \omega_i| \, dt, \quad t \in [t_0, t_n].
\tag{24}
$$

The calculation process of the objective function (24) to determine the optimal cross-sectional dimensions of the rods for the 3-RRR PPM is shown in Figure 2.

The constraint condition is

$$
\begin{cases}
\mathbf{w_{lb}} \le \mathbf{w} \le \mathbf{w_{ub}}, \\[2mm]
\mathbf{w_{lb}} = \begin{bmatrix} u_{1lb} & v_{1lb} & u_{2lb} & v_{2lb} & \dots & u_{7lb} & v_{7lb} \end{bmatrix}^T, \\[2mm]
\mathbf{w_{ub}} = \begin{bmatrix} u_{1ub} & v_{1ub} & u_{2ub} & v_{2ub} & \dots & u_{7ub} & v_{7ub} \end{bmatrix}^T,
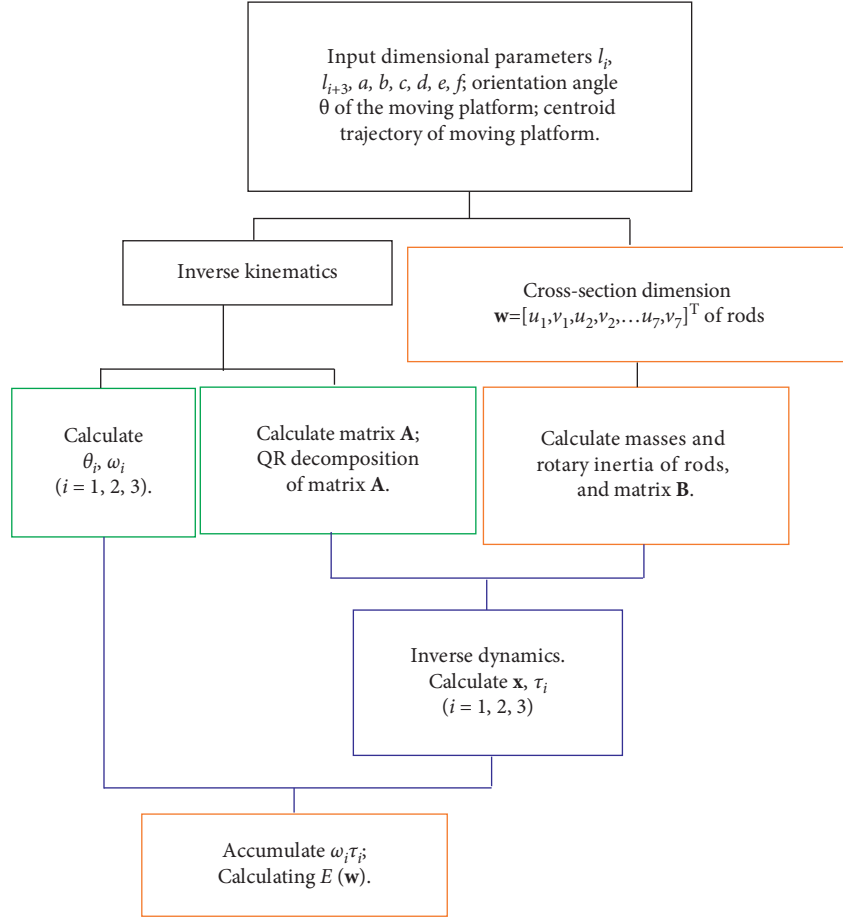\end{cases}
\tag{25}
$$

FIGURE 2: Calculation process of the objective function to determine the optimal cross-sectional dimension of the rods.

where $\mathbf{w_{lb}}$ and $\mathbf{w_{ub}}$ are the lower limit and the upper limit of $\mathbf{w}$, respectively.

3.2. Solving the Model of the Optimal Cross-Sectional Dimension of the Rods for the 3-RRR PPM Based on IBOA.

The BOA, which was inspired by the foraging behavior of butterflies, is a metaheuristic algorithm presented by Arora and Singh in 2018; in particular, the BOA is more efficient than other metaheuristic algorithms for solving engineering problems [30, 31]. It is assumed that every butterfly can emit fragrance and attract each other through fragrance; the BOA's key is the concept of fragrance and perception, which is expressed through the power exponent of stimulus intensity as follows [30, 31]:

$$f_k = c' I_k^{a'},\qquad(26)$$

where f_k ($k = 1, 2, \ldots, n$) is the fragrance of kth butterfly and I_k, which is defined by the objective function (24) with $w_k(u_k, v_k)$ representing the stimulus intensity; in addition, the power exponent a' and the sensory modality c' are real numbers in the range [0, 1].

There are two types of iterative patterns in seeking the optimal objective function (24) in the BOA; that is, the global or local search ensures that any butterfly can move randomly or toward the best butterfly that emits more fragrance. The iterative formula for the global search is [30, 31]

$$w_k^{t+1} = w_k^t + \left(r^2 \times w^* - w_k^t\right) \times f_k,\qquad(27)$$

where w^* is the current best solution among $w_k(u_k, v_k)$ ($k = 1, 2, \ldots, n$) in the current iteration, t is the number of iterations, and r is a random number in [0, 1]. The iterative formula for the local search is [30, 31]

$$w_k^{t+1} = w_k^t + \left(r^2 \times w_j^t - w_k^t\right) \times f_k,\qquad(28)$$

where $j \in \{1, 2, \ldots, n\}$.

The problem of the optimal cross-sectional dimension of rods for the 3-RRR PPM in this study is a constrained single-object optimization because there are difficulties in the process of changing to unconstrained multiobjective optimization; for example, the penalty function is exceedingly sensitive to penalty factors [32, 33]. Therefore, to properly handle the constraints of the single-object optimization problem, the IBOA is presented. To ensure that the new point iterated always falls into the feasible region, two measures are used in the IBOA, as follows:

(1) When the initial population of n butterflies is generated, $\mathbf{w}_k$ ($k = 1, 2, \ldots, n$) is randomly determined in the feasible region of equation (25):

$$w_{kl} = \frac{w_{lbl} + \lambda_{kl} w_{ubl}}{1 + \lambda_{kl}}, \tag{29}$$

where $k = 1, 2, 3, \ldots, n$ and $l = 1, 2, 3, \ldots, 14$. w_{lbl} and w_{ubl} are lth components of $\mathbf{w_{lb}}$ and $\mathbf{w_{ub}}$, w_{kl} is lth component of $\mathbf{w_k}$, and $\lambda_{kl} \in [0, 100]$ is the ratio (a random number) when $\mathbf{w_k}$ is calculated according to the formula of definite proportional division point. Meanwhile, the population size n was 50 in literature [31], and the condition that n is greater than 100 is also requested in this paper to ensure population diversity.

(2) After the global or local iteration has been executed, it is estimated whether the new point iterated falls into the feasible region of equation (25) or not through if-else control flow. The subsequent operation is executed if the new point iterated falls into the feasible region of equation (25), whereas the new iterated point is replaced by the current best solution w^* if the new point iterated does not fall into the feasible region of equation (25).

The terminal condition of iteration is as follows:

$$t \leq t_{\max} \text{ or } \left\| E(\mathbf{w}^*)^t - E(\mathbf{w}^*)^{t-1} \right\| \leq 1e - 5. \tag{30}$$

where $t_{\max}$ is the maximum number of iterations and $E(w^*)^t$ is the value of the objective function corresponding to the best solution $\mathbf{w}^*$ in the tth iteration.

The program flowchart of using IBOA to solve the problem of optimal cross-sectional dimensions of rods for the 3-RRR PPM is shown in Figure 3 (in which red lines are added in the improved parts of BOA).

4. Example, Solving, Experimental Verification, and Discussion

4.1. Example and Solving. As shown in Figure 1(a), the dimension parameters for the 3-RRR PPM were $\Sigma = a + b + c = 0.2533$ m, $a/\Sigma = 0.2096$, $b/\Sigma = 0.3628$, $c/\Sigma = 0.4276$, $l_1/\Sigma = 0.0750$, $l_2/\Sigma = 0.0553$, $l_3/\Sigma = 0.0632$, $l_4/\Sigma = 0.1382$, $l_5/\Sigma = 0.1342$, $l_6/\Sigma = 0.2132$, $d/\Sigma = 0.1733$, $e/\Sigma = 0.1899$, and $f/\Sigma = 0.1141$. The material density of the rods was $\rho = 2700$ kg/m^3.

A spring was used to connect the central point G_7 of the moving platform and another point with coordinates (0.09, 0.09) (unit: m) on the frame, and the elastic coefficient and free length of the spring were $K = 20$ and $l_0 = 0.015$ m. The external moment M_e of the moving platform was zero, and the external force F_e via the center of mass of the moving platform was

$$\mathbf{F}_e = \begin{bmatrix} F_{ex} \\ F_{ey} \end{bmatrix} = \frac{K\left(\sqrt{(q_1 - x)^2 + (q_2 - y)^2} - l_0\right)}{\sqrt{(q_1 - x)^2 + (q_2 - y)^2}} \begin{bmatrix} q_1 - x \\ q_2 - y \end{bmatrix}, \tag{31}$$

where the units of x and y are meters.

The working mode was "--+" for the 3-RRR PPM, orientation angle θ of the moving platform was 0 rad, which is not singular [11], and global coordinates of the central point G_7 of the moving platform were as follows [11, 21]:

$$\begin{cases} x = 0.010\left(1 - \dfrac{t}{15}\right)\cos(\omega\pi t), \\ \\ y = 0.025 + 0.010\left(1 - \dfrac{t}{15}\right)\sin(\omega\pi t), \end{cases} \quad t \in [0, T]. \tag{32}$$

Here, $T = 15$ s. The workspace of the 3-RRR PPM and the spiral trajectory of central point G_7 of the moving platform under "--+" working mode and $\theta = 0$ rad are shown in Figure 4.

Let $p = 0.5$, $c' = 0.2$, $t_{\max} = 350$, $\mathbf{w_{lb}} = 10^{-3}$ [15, 5, 15, 5, 15, 5, 15, 5, 15, 5, 15, 5, 15, 5]^T (unit: m), and $\mathbf{w_{ub}} = 10^{-3}$ [30, 10, 30, 10, 30, 10, 30, 10, 30, 10, 30, 10, 30, 10]^T (unit: m). In the initial population of n butterflies, $n = 110$, a', and $r \in [0, 1]$ were updated by a random number according to Figure 3 during the running of the program. The program based on Figure 3 was run, and the minimum of the objective function $\mathbf{E}(w)$ was 0.0764 J when the number of iterations was 107, and the best solution corresponding to the minimum of the objective function $\mathbf{w^*_{best}} = [0.015, 0.005, 0.015, 0.005, 0.015, 0.005, 0.03, 0.01, 0.03, 0.01, 0.03, 0.01, 0.015, 0.005]^T$ (unit: m).

As is shown in Figure 3, the algorithmic complexity of the proposed IBOA in comparison with the BOA is approximately equal to that of the BOA for the following reasons. Double loops in which the number of outer loops is n and the number of inner loops is 14 can be used during generating the initial population of n butterflies according to equation (29), and this operation has little influence on time and space complexity. In addition, after the global or local iteration has been executed in the BOA, an if-else control flow was added to estimate whether the new point iterated falls into the feasible region of equation (25) or not, and this operation does not add space complexity and has little influence on time complexity. In view of the fact that the BOA has been benchmarked [31], combining the algorithmic complexity analysis of the IBOA, the IBOA will be verified through comparing the IBOA with PSO [21] and BOA [30, 31] and through further experimental verification of physical prototype.

The reason why the PSO and BOA were chosen as benchmarking algorithms is that PSO was used to optimize the link and platform masses for minimizing the electrical energy consumption [21] and BOA was also applied to solve 6 familiar engineering problems [31]. The comparisons among the IBOA, PSO, and BOA were implemented in order to obtain fair results under the following conditions: the population sizes of the IBOA, PSO, and BOA were set as 110, and all initial population was randomly generated according to equation (29); the parameters of the PSO such as the constriction factor, inertia weight, and positive acceleration constants were set according to literature [21], and
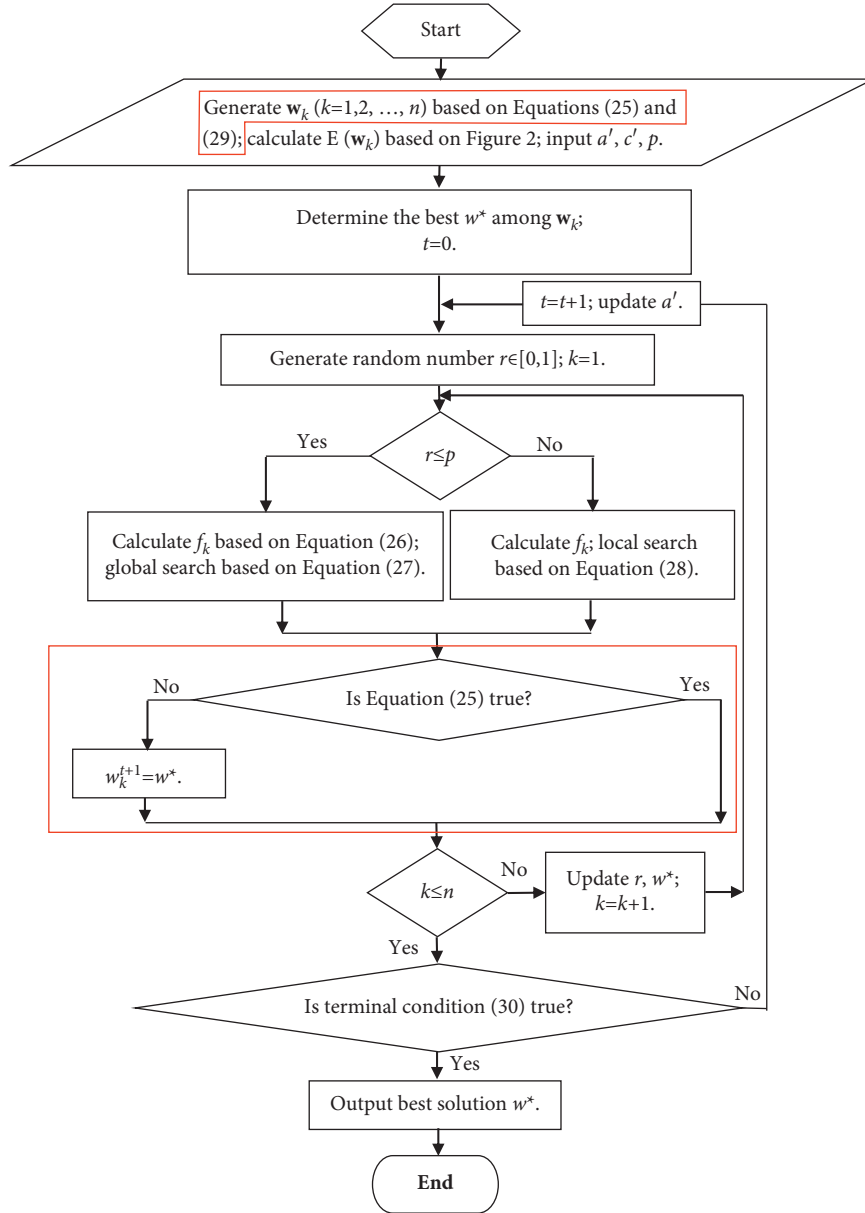
Figure 3: Program flowchart of using IBOA to solve the problem of optimal cross-sectional dimension of rods for the 3-RRR PPM.

the parameters of BOA and IBOA were the same as those previously mentioned.

The convergence curves of the three algorithms are shown in Figure 5. The total number of iterations of the IBOA, PSO, and BOA is 107, 90, and 128, respectively; the value of the objective function at the end of the iteration is 0.0764 J, 0.1070 J, and 0.0766 J. And the IBOA is 40 percent more accurate than the PSO and 0.29 percent more accurate than the BOA. Although the IBOA is a little more accurate than the BOA, the former is smaller in the total number of iterations. Therefore, the IBOA is more suitable than the PSO and BOA for solving the engineering optimization problems in this paper.

4.2. Experimental Verification and Discussion. The experimental verification system is shown in Figure 6, where the mechanical, control, and test systems of the 3-RRR PPM include a 3-RRR PPM, a personal computer (PC), three servomotors, three matched servomotor drivers of the type TSC06401C2NL/TSTA20 C, and three torque/speed sensors of the type PPCI-L112/JN338-2VE. According to the RS-485 serial bus standard, the 3-RRR PPM is operated by Visual C++ programming [11, 24].

According to the optimal section dimensions of the rods, $w_{\text{best}}^* = [0.015, 0.005, 0.015, 0.005, 0.015, 0.005, 0.03, 0.01, 0.03, 0.01, 0.03, 0.01, 0.015, 0.005]^{\text{T}}$ (unit: m). First, the 3-RRR PPM was assembled, and the test was then conducted.
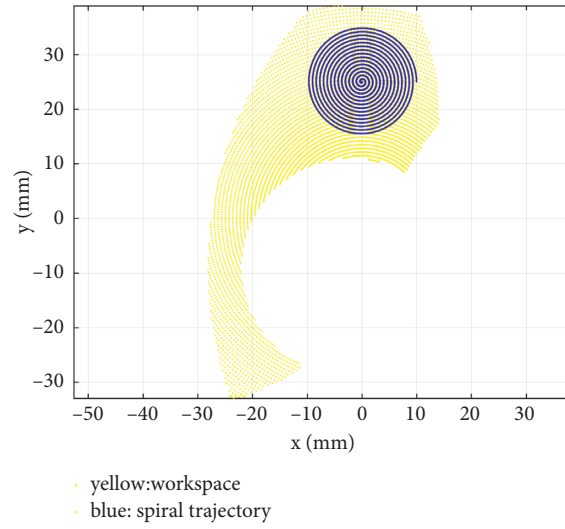
FIGURE 4: Workspace of the 3-RRR PPM and the spiral trajectory of central point G_7 under "--+" working mode and $\theta = 0$ rad.
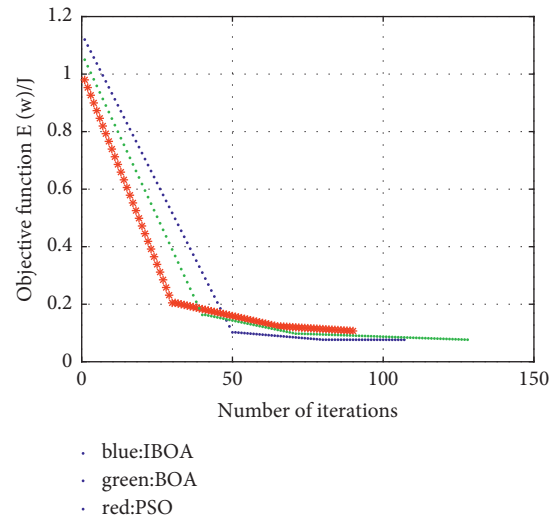

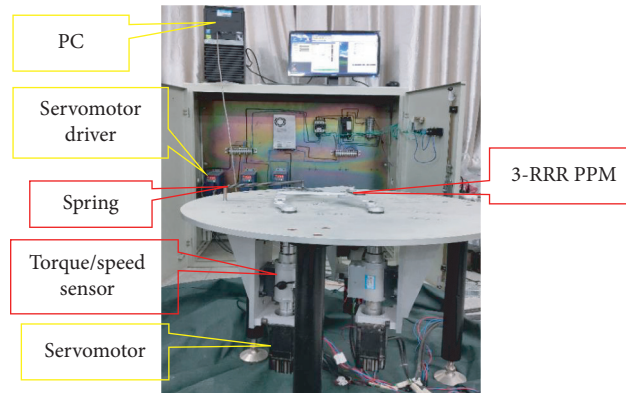FIGURE 5: Convergence figure of the IBOA, BOA, and PSO.

FIGURE 6: Experimental verification system.

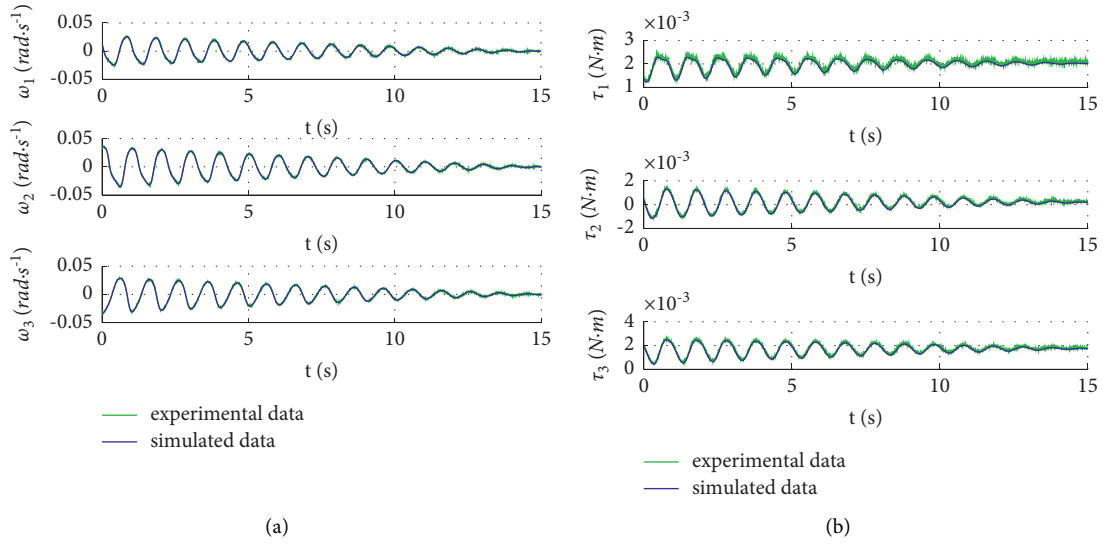(a)   (b)

Figure 7: (a) Comparison of the simulation and experiment for the angular velocities of the active rod A_iB_i; (b) comparison of the simulation and experiment for the driving moment of the active rod A_iB_i.
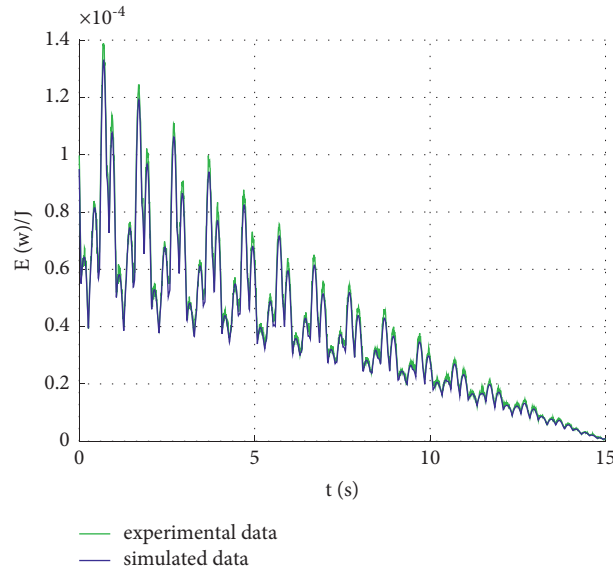
Figure 8: Comparison of the simulation and experiment for the energy consumption of the 3-RRR PPM.

After the torque/speed sensor data are obtained, the comparative results of the simulation and experiment for the angular velocities of the active rod A_iB_i are shown in Figure 7(a), and the comparative results of the simulation and experiment for the driving moment of the active rod A_iB_i are shown in Figure 7(b). The comparative results of the simulation and experiment for the energy consumption of the 3-RRR PPM are shown in Figure 8.

Employing numerical integration, the total simulation energy consumption was 0.0764 J, and the total experimental energy consumption was 0.0794 J. The latter is slightly larger than the former, and the error is 0.0030 J mainly because the friction dissipation energy of the hinges

is not included in the energy consumption model of equation (24). Therefore, the error between the total experimental energy consumption and the total simulation energy consumption based on the optimal solution by the IBOA is within the expected range. The results show that the dynamics model based on the Newton–Euler method, numerical solving for the dynamical model of the 3-RRR PPM based on QR decomposition, and numerical solving for optimal cross-sectional dimension of rods to minimize energy consumption based on the IBOA are reasonable and in accordance with the engineering practice. Furthermore, the comparison among the IBOA, PSO, and BOA and experiment results of the physical prototype for the 3-RRR

TABLE 1: Parameters of dimension, kinematics, and dynamics for the 3-RRR PPM (where $i = 1, 2, 3$).

Meaning	Symbol
Distance between hinge axes A_1 and A_2	a
Distance between hinge axes A_2 and A_3	b
Distance between hinge axes A_3 and A_1	c
Distance between hinge axes C_1 and C_2	d
Distance between hinge axes C_2 and C_3	e
Distance between hinge axes C_3 and C_1	f
Lengths of the active rods A_iB_i	l_i
Length of the passive rod B_iC_i	l_{i+3}
Global coordinates of the points A_i	(x_{Ai}, y_{Ai})
Global coordinates of the points B_i	(x_{Bi}, y_{Bi})
Global coordinates of the points C_i	(x_{Ci}, y_{Ci})
Local coordinates of the points C_i	$(x_{Ci'}, y_{Ci'})$
Global coordinate of the central point G_7 of the moving platform	(x, y)
Global coordinates of the points G_i	(x_{Gi}, y_{Gi})
Global coordinates of the points $G_{(i+3)}$	$(x_{G(i+3)}, y_{G(i+3)})$
Orientation angle of the moving platform	Θ
Rotation angle of the active rod A_iB_i	θ_i
Angular velocities of the active rod A_iB_i	ω_i
Rotation angle of the passive rod B_iC_i	θ_{i+3}
Angular acceleration of the active rod A_iB_i	α_{Gi}
Angular acceleration of the passive rod B_iC_i	$\alpha_{G(i+3)}$
Angular acceleration of the moving platform	α_{G7}
Acceleration of the central points G_i of the active rod A_iB_i	$\mathbf{a}_{Gi}$
Acceleration of the central points $G_{(i+3)}$ of the passive rod B_iC_i	$\mathbf{a}_{G(i+3)}$
Acceleration of the central point G7 of the moving platform	$\mathbf{a}_{G7}$
Masses of the active rod A_iB_i	m_{Gi}
Masses of the passive rod B_iC_i	$m_{G(i+3)}$
Masses of the moving platform	m_{G7}
The x-direction inertia forces of the active rod A_iB_i	F_{Gix}
The y-direction inertia forces of the active rod A_iB_i	F_{Giy}
The x-direction inertia forces of the passive rod B_iC_i	$F_{G(i+3)x}$
The y-direction inertia forces of the passive rod B_iC_i	$F_{G(i+3)y}$
The x-direction inertia forces of the moving platform	F_{G7x}
The y-direction inertia forces of the moving platform	F_{G7y}
Rotary inertia round the centroidal axis of the active rod A_iB_i	J_{Gi}
Rotary inertia round the centroidal axis of the passive rod B_iC_i	$J_{G(i+3)}$
Rotary inertia round the centroidal axis of the moving platform	J_{G7}
Moment of inertia of the active rod A_iB_i	M_{Gi}
Moment of inertia of the passive rod B_iC_i	$M_{G(i+3)}$
Moment of inertia of the moving platform	M_{G7}
The x-direction external force of the moving platform	F_{ex}
The y-direction external force of the moving platform	F_{ey}
External moment of the moving platform	M_e
The x-direction internal forces at the point B_i	F_{Bix}
The y-direction internal forces at the point B_i	F_{Biy}
The x-direction internal forces at the point C_i	F_{Cix}
The y-direction internal forces at the point C_i	F_{Ciy}
Driving moments of the active rod A_iB_i	τ_i

PPM indicate that the IBOA is suitable for solving the constrained single-object optimization problem and has great potential in solving the optimization problems in engineering practice.

5. Conclusions

The comparisons between the simulation energy consumption based on the optimal solution by the IBOA and the experimental energy consumption from physical prototype of the 3-RRR PPM show that the dynamics model based on the Newton–Euler method, numerical solving for the dynamical model of the 3-RRR PPM based on QR decomposition, and numerical solving for optimal cross-sectional dimension of rods to minimize energy consumption based on the IBOA are reasonable and in accordance with the engineering practice.

The proposed IBOA abandons the constraints processing scheme of transforming constrained single-objective optimization problems into unconstrained multiobjective optimization problems. In the IBOA, the initial population is randomly generated. More importantly, after the global or local search in the BOA, the newly generated iteration point is immediately

judged: whether it falls into the feasible region or not. Then, the newly generated iteration points out of the feasible region are replaced by the current optimal points. The results of comparison among the IBOA, PSO, and BOA and experiment results of the physical prototype for the 3-RRR PPM show that the IBOA is suitable for solving the constrained single-object optimization problems and has great potential in the convergence speed and accuracy to solve the optimization problems in engineering practice.

Appendix

A. Meaning and Symbols of Parameters

Parameters of dimension, kinematics, and dynamics for the 3-RRR PPM are shown in Table 1.

B. Formulae of Geometry, Kinematics, and Dynamics for 3-RRR PPM

Computational formulae related to the parameters of dimension, kinematics, and dynamics (where, $i = 1, 2, 3$) [11, 24] are as follows:

(1) The parameters of dimension and the coordinate of the points

$$x_{Ai} = \begin{cases} \dfrac{a^2 - c^2}{3b}, & i = 1, \\[2mm] -\dfrac{3b^2 + a^2 - c^2}{6b}, & i = 2, \\[2mm] \dfrac{3b^2 + c^2 - a^2}{6b}, & i = 3, \end{cases} \tag{B.1}$$

$$y_{Ai} = \begin{cases} \dfrac{2}{3}h_2, & i = 1, \\[2mm] -\dfrac{1}{3}h_2, & i = 2, 3, \end{cases} \tag{B.2}$$

where h_2 is the height on the side A_2A_3 of triangle $A_1A_2A_3$.

$$x'_{Ci} = \begin{cases} \dfrac{d^2 - f^2}{3e}, & i = 1, \\[2mm] -\dfrac{3e^2 + d^2 - f^2}{6e}, & i = 2, \\[2mm] \dfrac{3e^2 + f^2 - d^2}{6e}, & i = 3, \end{cases} \tag{B.3}$$

$$y'_{Ci} = \begin{cases} \dfrac{2}{3}h'_2, & i = 1, \\[2mm] -\dfrac{1}{3}h'_2, & i = 2, 3, \end{cases} \tag{B.4}$$

where h_2' is the height on the side C_2C_3 of triangle $C_1C_2C_3$.

$$\begin{bmatrix} x_{Bi} \\ y_{Bi} \end{bmatrix} = \begin{bmatrix} x_{Ai} + l_i \ \cos\theta_i \\ y_{Ai} + l_i\sin\theta_i \end{bmatrix}, \tag{B.5}$$

$$\begin{bmatrix} x_{Ci} \\ y_{Ci} \end{bmatrix} = \begin{bmatrix} x \\ y \end{bmatrix} + \begin{bmatrix} \cos\theta & -\sin\theta \\ \sin\theta & \cos\theta \end{bmatrix} \begin{bmatrix} x'_{Ci} \\ y'_{Ci} \end{bmatrix}, \tag{B.6}$$

$$\begin{bmatrix} x_{Gix} \\ x_{Giy} \end{bmatrix} = \frac{1}{2}\begin{bmatrix} x_{Ai} + x_{Bi} \\ y_{Ai} + y_{Bi} \end{bmatrix}, \tag{B.7}$$

$$\begin{bmatrix} x_{G(i+3)x} \\ x_{G(i+3)y} \end{bmatrix} = \frac{1}{2}\begin{bmatrix} x_{Ci} + x_{Bi} \\ y_{Ci} + y_{Bi} \end{bmatrix}. \tag{B.8}$$

(2) The parameters of kinematics

$$\omega_i = \dot{\theta}_i, \tag{B.9}$$

$$\theta_{i+3} = \arccos\frac{\mathbf{B_i C_i} \cdot (1,0)}{l_{i+3}}, \tag{B.10}$$

$$\alpha_{Gi} = \ddot{\theta}_i, \tag{B.11}$$

$$\alpha_{G(i+3)} = \ddot{\theta}_{i+3}, \tag{B.12}$$

$$\alpha_{G7} = \ddot{\theta}, \tag{B.13}$$

$$\mathbf{a}_{Gi} = \begin{bmatrix} a_{Gix} \\ a_{Giy} \end{bmatrix} = \begin{bmatrix} \ddot{x}_{Gi} \\ \ddot{y}_{Gi} \end{bmatrix}, \tag{B.14}$$

$$\mathbf{a}_{G(i+3)} = \begin{bmatrix} a_{G(i+3)x} \\ a_{G(i+3)y} \end{bmatrix} = \begin{bmatrix} \ddot{x}_{G(i+3)} \\ \ddot{y}_{G(i+3)} \end{bmatrix}, \tag{B.15}$$

$$\mathbf{a}_{G7} = \begin{bmatrix} \ddot{x} \\ \ddot{y} \end{bmatrix}. \tag{B.16}$$

(3) The parameters of dynamics

$$\begin{bmatrix} F_{Gix} \\ F_{Giy} \end{bmatrix} = -m_{Gi}\begin{bmatrix} a_{Gix} \\ a_{Giy} \end{bmatrix}, \tag{B.17}$$

$$\begin{bmatrix} F_{G(i+3)x} \\ F_{G(i+3)y} \end{bmatrix} = -m_{G(i+3)}\begin{bmatrix} a_{G(i+3)x} \\ a_{G((i+3)y} \end{bmatrix}, \tag{B.18}$$

$$\begin{bmatrix} F_{G7x} \\ F_{G7y} \end{bmatrix} = -m_{G7}\begin{bmatrix} a_{G7x} \\ a_{G7y} \end{bmatrix}, \tag{B.19}$$

$$M_{Gi} = -J_{Gi}\alpha_i, \tag{B.20}$$

$$M_{G(i+3)} = -J_{G(i+3)}\alpha_{G(i+3)}, \tag{B.21}$$

$$M_{G7} = -J_{G7}\alpha_{G7}, \tag{B.22}$$

where

$$J_{Gi} = \frac{m_{Gi}l_i^2}{12}, \tag{B.23}$$

$$J_{G(i+3)} = \frac{m_{G(i+3)}l_{i+3}^2}{12}, \tag{B.24}$$

$$J_{G7} = \frac{m_{G7}}{2}\frac{d^3 + e^3 + f^3 + 3def}{d + e + f}. \tag{B.25}$$

Data Availability

The data used to support the findings of this study are available from the corresponding author upon request.

Conflicts of Interest

The authors declare that they have no conflicts of interest.

Acknowledgments

References

[1] E. Can and H. Stachel, "A planar parallel 3-RRR robot with synchronously driven cranks," *Mechanism and Machine Theory*, vol. 79, pp. 29–45, 2014.

[2] P. H. Hu, Y. J. Li, and Q. C. Zhao, "Development of micro-force sensor based on 3-RRR parallel mechanism," *Applied Mechanics and Materials*, vol. 36, pp. 57–62, 2010.

[3] S. Šalinić and A. Nikolić, "A new pseudo-rigid-body model approach for modeling the quasi-static response of planar flexure-hinge mechanisms," *Mechanism and Machine Theory*, vol. 124, pp. 150–161, 2018.

[4] M. Farajtabar, H. M. Daniali, and S. M. Varedi, "Pick and place trajectory planning of planar 3-RRR parallel manipulator in the presence of joint clearance," *Robotica*, vol. 35, no. 2, pp. 241–253, 2017.

[5] S. M. Varedi-Koulaei, H. M. Daniali, M. Farajtabar, B. Fathi, and M. Shafiee-Ashtiani, "Reducing the undesirable effects of joints clearance on the behavior of the planar 3-RRR parallel manipulators," *Nonlinear Dynamics*, vol. 86, no. 2, pp. 1007–1022, 2016.

[6] R. Fisher, R. P. Podhorodeski, and S. B. Nokleby, "Design of a reconfigurable planar parallel manipulator," *Journal of Robotic Systems*, vol. 21, no. 12, pp. 665–675, 2004.

[7] G. Liu, Y. Wang, Y. Zhang, and Z. Xie, "Real-time solution of the forward kinematics for a parallel haptic device using a numerical approach based on neural networks," *Journal of Mechanical Science and Technology*, vol. 29, no. 6, pp. 2487–2499, 2015.

[8] H. Lamine and L. Houssein, "Comparative kinematic analysis and design optimization of redundant and nonredundant planar parallel manipulators intended for haptic use," *Robotica*, vol. 38, no. 8, pp. 1463–1477, 2020.

[9] G. Wu and S. Bai, "Design and kinematic analysis of a 3-RRR spherical parallel manipulator reconfigured with four-bar linkages," *Robotics and Computer-Integrated Manufacturing*, vol. 56, pp. 55–65, 2019.

[10] W. Ye, Y. Fang, and S. Guo, "Design and analysis of a reconfigurable parallel mechanism for multidirectional additive manufacturing," *Mechanism and Machine Theory*, vol. 112, pp. 307–326, 2017.

[11] Y. Gao, K. Chen, H. Gao, P. Xiao, and L. Wang, "Small-angle perturbation method for moving platform orientation to avoid singularity of asymmetrical 3-RRR planner parallel manipulator," *Journal of the Brazilian Society of Mechanical Sciences and Engineering*, vol. 41, no. 12, 2019.

[12] Z. Shao, X. Tang, and X. Chen, "Inertia match of a 3-RRR reconfigurable planar parallel manipulator," *Chinese Journal of Mechanical Engineering*, vol. 22, no. 6, pp. 791–799, 2009.

[13] J. X. Yang, Z. T. Liu, and J. W. Sun, "Dynamic modeling of overconstrained parallel robot," *Applied Mechanics and Materials*, vol. 373–375, pp. 34–37, 2013.

[14] A. Cammarata, "A novel method to determine position and orientation errors in clearance-affected overconstrained mechanisms," *Mechanism and Machine Theory*, vol. 118, pp. 247–264, 2017.

[15] J. Angeles, O. Ma, and A. Rojas, "An algorithm for the inverse dynamics of n-axis general manipulators using Kane's equations," *Computers & Mathematics with Applications*, vol. 17, no. 12, pp. 1545–1561, 1989.

[16] Y.-Q. Yu, Z.-C. Du, J.-X. Yang, and Y. Li, "An experimental study on the dynamics of a 3-RRR flexible parallel robot," *IEEE Transactions on Robotics*, vol. 27, no. 5, pp. 992–997, 2011.

[17] S. Staicu, "Matrix modeling of inverse dynamics of spatial and planar parallel robots," *Multibody System Dynamics*, vol. 27, no. 2, pp. 239–265, 2012.

[18] M. Koul, S. V. Shah, S. K. Saha, and M. Manivannan, "Reduced-order forward dynamics of multiclosed-loop systems," *Multibody System Dynamics*, vol. 31, no. 4, pp. 451–476, 2014.

[19] J. Wu, J. Wang, and Z. You, "A comparison study on the dynamics of planar 3-DOF 4-RRR, 3-RRR and 2-RRR parallel manipulators," *Robotics and Computer-Integrated Manufacturing*, vol. 27, no. 1, pp. 150–156, 2011.

[20] J. V. Fontes and M. M. da Silva, "On the dynamic performance of parallel kinematic manipulators with actuation and kinematic redundancies," *Mechanism and Machine Theory*, vol. 103, pp. 148–166, 2016.

[21] S. Kucuk, "Energy minimization for 3-RRR fully planar parallel manipulator using particle swarm optimization," *Mechanism and Machine Theory*, vol. 62, no. 4, pp. 129–149, 2013.

[22] X. Zhang, X. Zhang, and Z. Chen, "Dynamic analysis of a 3-RRR parallel mechanism with multiple clearance joints," *Mechanism and Machine Theory*, vol. 78, pp. 105–115, 2014.

[23] X. Zhang and X. Zhang, "A comparative study of planar 3-RRR and 4-RRR mechanisms with joint clearances," *Robotics and Computer-Integrated Manufacturing*, vol. 40, pp. 24–33, 2016.

[24] Y. Gao, K. Chen, H. Gao, H. Zheng, L. Wang, and P. Xiao, "Energy consumption prediction for 3-RRR PPM through combining LSTM neural network with Whale optimization algorithm," *Mathematical Problems in Engineering*, vol. 2020, Article ID 6590397, 17 pages, 2020.

[25] T. Terao, K. Ozaki, and T. Ogita, "LU-Cholesky QR algorithms for thin QR decomposition," *Parallel Computing*, vol. 92, pp. 102571–102611, 2020.

[26] A. W. Mohamed, A. A. Hadi, and A. K. Mohamed, "Gaining-sharing knowledge based algorithm for solving optimization problems: a novel nature-inspired algorithm," *International Journal of Machine Learning and Cybernetics*, vol. 11, no. 7, pp. 1501–1529, 2020.

[27] W. Deng, J. Xu, X.-Z. Gao, and H. Zhao, "An enhanced MSIQDE algorithm with novel multiple strategies for global optimization problems," *IEEE Transactions on Systems, Man, and Cybernetics: Systems*, vol. 2020, Article ID 3030792, 10 pages, 2020.

[28] W. Deng, J. Xu, H. Zhao, and Y. Song, "A novel gate resource allocation method using improved PSO-based QEA," *IEEE Transactions on Intelligent Transportation Systems*, vol. 2020, Article ID 3025796, 9 pages, 2020.

[29] W. Deng, S. Shang, X. Cai et al., "Quantum differential evolution with cooperative coevolution framework and hybrid mutation strategy for large scale optimization," *Knowledge-Based Systems*, vol. 224, Article ID 107080, 2021.

[30] S. Arora, S. Singh, and K. Yetilmezsoy, "A modified butterfly optimization algorithm for mechanical design optimization problems," *Journal of the Brazilian Society of Mechanical Sciences and Engineering*, vol. 40, no. 1, 2018.

[31] S. Arora and S. Singh, "Butterfly optimization algorithm: a novel approach for global optimization," *Soft Computing*, vol. 23, no. 3, pp. 715–734, 2019.

[32] A. H. Aguirre, S. B. Rionda, C. A. Coello Coello, G. L. Lizárraga, and E. M. Montes, "Handling constraints using multiobjective optimization concepts," *International Journal for Numerical Methods in Engineering*, vol. 59, no. 15, pp. 1989–2017, 2004.

[33] C. Segura, C. A. Coello Coello, G. Miranda, and C. León, "Using multi-objective evolutionary algorithms for single-objective optimization," *4OR*, vol. 11, no. 3, pp. 201–228, 2013.

[34] R. Chai, A. Savvaris, A. Tsourdos, Y. Xia, and S. Chai, "Solving multiobjective constrained trajectory optimization problem by an extended evolutionary algorithm," *IEEE Transactions on Cybernetics*, vol. 50, no. 4, pp. 1630–1643, 2020.